Mechanism of allosteric inhibition in the *Plasmodium falciparum* cGMP-dependent protein kinase

Jung Ah Byun[‡], Katherine Van[‡], Jinfeng Huang[§], Philipp Henning[¶], Eugen Franz[||], Madoka Akimoto[§], Friedrich W. Herberg[¶], Choel Kim[**‡‡], and Giuseppe Melacini[‡§1]

From the Departments of [‡]Biochemistry and Biomedical Sciences and [§]Chemistry and Chemical Biology, McMaster University, Hamilton, Ontario L8S 4L8, Canada, the [¶]Department of Biochemistry, University of Kassel, Heinrich-Plett-Strasse 40, 34132 Kassel, Germany, [||]Biaffin GmbH & Co. KG, Heinrich-Plett-Strasse 40, 34132 Kassel, Germany, and the [**]Verna and Marrs McLean Department of Biochemistry and Molecular Biology and [‡‡]Department of Pharmacology and Chemical Biology, Baylor College of Medicine, Houston, Texas 77030

Edited by Wolfgang Peti

Most malaria deaths are caused by the protozoan parasite *Plasmodium falciparum*. Its life cycle is regulated by a cGMP-dependent protein kinase (*Pf*PKG), whose inhibition is a promising antimalaria strategy. Allosteric kinase inhibitors, such as cGMP analogs, offer enhanced selectivity relative to competitive kinase inhibitors. However, the mechanisms underlying allosteric *Pf*PKG inhibition are incompletely understood. Here, we show that 8-NBD-cGMP is an effective *Pf*PKG antagonist. Using comparative NMR analyses of a key regulatory domain, *Pf*D, in its *apo*, cGMP-bound, and cGMP analog–bound states, we elucidated its inhibition mechanism of action. Using NMR chemical shift analyses, molecular dynamics simulations, and site-directed mutagenesis, we show that 8-NBD-cGMP inhibits *Pf*PKG not simply by reverting a two-state active *versus* inactive equilibrium, but by sampling also a distinct inactive "mixed" intermediate. Surface plasmon resonance indicates that the ability to stabilize a mixed intermediate provides a means to effectively inhibit *Pf*PKG, without losing affinity for the cGMP analog. Our proposed model may facilitate the rational design of *Pf*PKG-selective inhibitors for improved management of malaria.

Malaria is a serious health risk for about 40% of the world's population, with more than 200 million diagnoses and 400,000 deaths globally estimated in 2018 (1). Most malarial deaths are caused by *Plasmodium falciparum* with life cycles in both the human and the mosquito hosts (2, 3). The regulation of such cycles relies on cyclic nucleotide signaling pathways (4). Specifically, the *P. falciparum* guanosine-3′,5′-cyclic monophosphate (cGMP)[2]-dependent kinase (*Pf*PKG) plays a major role in both replication and transmission of the *Plasmodium* parasite, including exflagellation and gametogenesis in the asexual blood stage, invasion of hepatocytes by sporozoites, and gliding motility of ookinetes (5–9). Hence, *Pf*PKG has emerged as a promising target for development of antimalaria therapies complementary to current malaria drugs, whose effectiveness is limited by increasing resistance (2, 10, 11). Furthermore, *Pf*PKG inhibition is an effective and novel strategy not only for malaria treatment, but also for malaria prophylaxis (2, 6, 12–15).

One strategy to inhibit *Pf*PKG is through targeting the active site in the kinase domain. Inhibitors that target such kinase active sites are effective, but poorly selective, because the active sites are highly conserved among eukaryotic kinases (16). One approach to circumvent this is to target allosteric sites, such as the cGMP-binding sites in *Pf*PKG.

*Pf*PKG consists of an N-terminal regulatory region followed by a C-terminal catalytic domain (Fig. 1*A*), similar to mammalian PKG (17–19). In the absence of cGMP, the regulatory region of *Pf*PKG autoinhibits the catalytic domain. Upon cGMP binding to the regulatory region, the *Pf*PKG autoinhibition is allosterically removed, resulting in activation. The regulatory domain is composed of four cGMP-binding domains (CBDs): A, B, C, and D (Fig. 1*A*). CBD-C is degenerate and does not bind to cGMP (20). CBD-D (here referred to as "*Pf*D") is adjacent to the catalytic domain (Fig. 1*A*) and exhibits the highest affinity and selectivity toward cGMP, with a K_d of 40 nM, compared with $K_d \geq 1$ μM for CBD-A and CBD-B (14). In addition, the construct spanning only *Pf*D and the catalytic domain displays low basal activity in the *apo* state and is efficiently activated by cGMP (21). Hence, *Pf*D serves as the critical controlling unit for both *Pf*PKG autoinhibition and activation.

[2] The abbreviations used are: cGMP, guanosine-3′,5′-cyclic monophosphate; *Pf*PKG, *P. falciparum* cGMP-dependent kinase; 8-NBD-cGMP, 8-(2-[7-nitro-4-benzofurazanyl]aminoethylthio)guanosine-3′,5′-cyclic monophosphate; 8-pCPT-cGMP, 8-(4-chlorophenylthio)guanosine-3′,5′-cyclic monophosphorothioate; PET-cGMP, β-phenyl-1,*N*²-ethenoguanosine-3′,5′-cyclic monophosphate; CBD, cyclic nucleotide–binding domain; BBR, base-binding region; PBC, phosphate-binding cassette; 2D, two-dimensional; CHESPA, chemical shift projection analysis; PDB, Protein Data Bank; HSQC, heteronuclear single quantum coherence; SPR, surface plasmon resonance; BME, β-mercaptoethanol; CCS, compounded ¹⁵N-¹H chemical shift; NTA, nitrilotriacetic acid.

*Pf*D is composed of a contiguous β-subdomain and noncontiguous α-subdomain (Fig. 1*B*) (14, 22). The β-subdomain forms a β-barrel critical for cGMP recognition and includes the base-binding region (BBR) and the phosphate-binding cassette (PBC) (Fig. 1, *B* and *C*), whereas the α-subdomain mediates inhibitory interactions with the catalytic domain and includes three N-terminal and two C-terminal helices, called the N3A motif and αB-αC, respectively (Fig. 1, *B* and *D*). In the *apo* form, the N3A contacts the β-barrel, whereas the C-terminal helices point away from it (Fig. 1*B*) (14). Upon cGMP binding, the N3A moves away from the β-subdomain, whereas the C-terminal helices are recruited to it by an arginine residue in the PBC, Arg[484] (Fig. 1*B*). Arg[484] bridges the PBC to two residues in the αC and defines a unique cGMP-capping triad (Fig. 1*B*), markedly distinct from human PKG, in which cGMP is capped by a Tyr in the C-terminal helix (23). Disruption of the *Pf*PKG-specific capping triad by mutations blocks proliferation in *P. falciparum* (14), confirming that *Pf*D is an excellent target for treating malaria. Additionally, Arg[528] in the αC plays a pivotal role in regulating *Pf*PKG activity by controlling the αC conformation through a hydrogen bond with Tyr[480], which stabilizes the active conformation (Fig. 1*D*) (14, 21, 24).

The allosteric transition of *Pf*D provides a simple model to rationalize the cGMP-dependent activation of the full-length protein through a four-state allosteric thermodynamic cycle, which arises from the coupling of the *Pf*D inactive-active autoinhibitory equilibrium and the *apo-holo* cGMP-binding equilibrium (Fig. 1*E*) (25–27). Of the four states (Fig. 1*E*), the *holo*-inactive is particularly relevant for inhibition. This state is selectively stabilized by partial agonists and/or antagonists, which decouple binding from the intramolecular allosteric pathways necessary for activation. We hypothesize that the stabilization of the *holo*-inactive state arise from a reversal of the two-state inactive/active conformational equilibrium (Fig. 1*F*) or from a multistate equilibrium sampling a distinct intermediate conformation that exhibits components of both the inactive and the active states of *Pf*D in different regions (Fig. 1*G*).

To test these hypotheses and understand the mechanism of action of allosteric partial agonists and antagonists that serve as leads for new *Pf*PKG-selective inhibitors, we use comparative NMR to analyze *Pf*D in its *apo*, cGMP-bound, and cGMP analog–bound forms. The cGMP analogs investigated here include 8-NBD-cGMP, 8-pCPT-cGMP, and PET-cGMP (Fig. 1, *I–K*). Our results reveal that 8-NBD-cGMP and 8-pCPT-cGMP significantly reduce the kinase activity and induce major perturbations throughout *Pf*D by stabilizing an additional intermediate conformer that is distinct from both the native *apo*-inactive and *holo*-active conformations. This "mixed" intermediate state exhibits inhibitory potential comparable with that of the *apo*-inactive state, as the C-terminal lid is disengaged, but it preserves an affinity similar to that of cGMP, as the key cGMP-binding regions, including the PBC and the adjacent αB, are still engaged. Hence, the stabilization of an allosterically mixed intermediate emerges as a new strategy for selectively inhibiting *Pf*PKG with high potency and efficacy.

Results and discussion

The apo versus cGMP-bound comparative NMR analyses of PfD reveal pervasive allosteric perturbations

As a first step to probe the allosteric effects of cGMP on the *Pf*D construct (residues 401–542) used in our NMR studies, we acquired NH HSQC spectra of *apo* and cGMP-bound *Pf*D (Fig. 2*A*). The cGMP-bound spectrum was assigned through triple-resonance NMR experiments and selective amino acid labeling. However, the *apo* construct was prone to precipitation during acquisition of 3D NMR data sets. Hence, the *apo* assignments were obtained by transferring the *holo* assignments to the *apo* spectrum through 2D N_z-exchange (Fig. 2, *B* and *D*) and 2D difference N_z-exchange experiments acquired in the presence of substoichiometric amounts of cGMP (Fig. 2, *C* and *E*). Based on these assignments, the cGMP-induced residue-specific compounded ^{15}N-^1H chemical shift changes (ΔCCS) were measured (Fig. 2*F*).

The majority of the residues exhibit significant ΔCCS values upon cGMP binding (Fig. 2*F*). As expected, significant ppm shifts are observed in the PBC and BBR regions, which directly interact with cGMP, as well as the β2–3 loop, which is adjacent to the PBC (Fig. 2*F*). Furthermore, major ppm changes are also detected for several α-helical regions, especially the αA, αB, and αC helices (Fig. 2*F*). The ppm shifts in αB-αC are consistent with the cGMP-dependent structural changes for these regions, as shown by the local root mean square deviation between the *apo* and cGMP-bound structures (Fig. 2*G*). The αB-αC structural changes also affect adjacent regions, such as the αA helix and the β8 strand (Fig. 2*F*), although such regions are not subject to major structural changes upon cGMP binding (Fig. 2*G*). Hence, the cGMP-dependent ΔCCS values (Fig. 2*F*) are in full agreement with the structures of *apo*- and *holo*-*Pf*D, providing an initial validation of our NMR assignments. Our NMR assignments were further validated by the agreement between the measured and the computed Cα and Cβ chemical shift values based on the *apo*- and *holo*-*Pf*D structures (Fig. 2, *H* and *I*). Once the NMR assignments were validated, we extended our analyses to evaluate the effects of cGMP analogs.

cGMP analog versus cGMP chemical shift differences report on inhibitory conformational changes of PfD

We focused on three cGMP base analogs with distinct base modifications: 8-NBD-, 8-pCPT-, and PET-cGMP (Fig. 1, *I–K*), as they act as *Pf*PKG activators to different degrees. Whereas PET-cGMP acts as an agonist, as shown by kinase assays (Fig. 1*L*), 8-pCPT- and 8-NBD-cGMP elicit progressively increasing potency as antagonists. 8-NBD-cGMP is the most potent inhibitor of *Pf*PKG (Fig. S1), followed by 8-pCPT-cGMP. This range of kinase responses (Fig. 1*L*) makes this group of cGMP analogs an excellent toolset to investigate the mechanisms underlying the allosteric inhibition of *Pf*PKG. For this purpose, we first measured the cGMP analog *versus* cGMP differences in compounded chemical shifts (Fig. 3*A*). The overall distributions of such ppm differences (Fig. 3*B*) rank in full agreement with the inhibitory potencies of the cGMP analogs (Fig. 1*L*). Furthermore, the
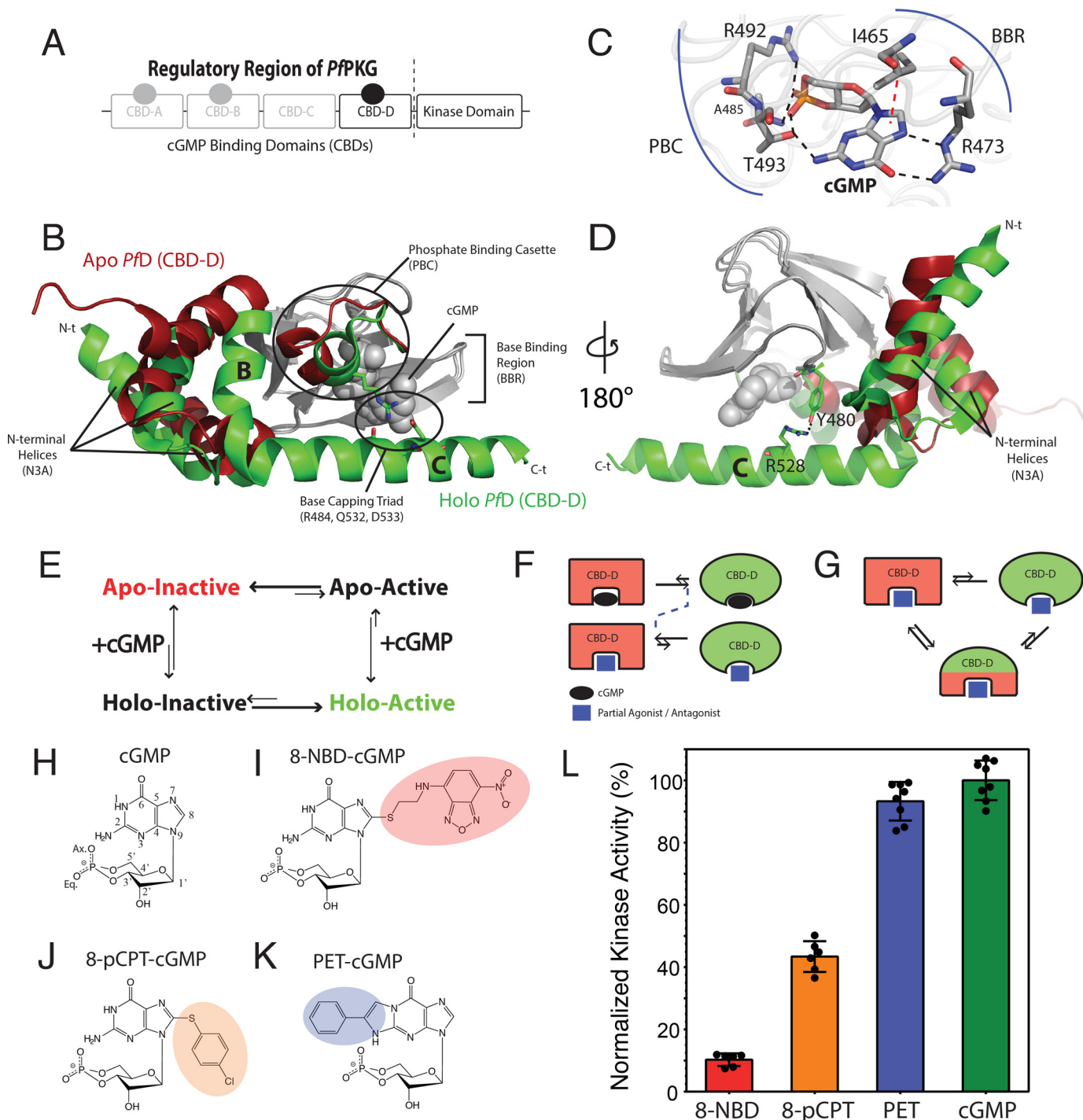
Figure 1. Structural architecture of *Pf*CBD-D and hypothetical models of inhibition. *A*, domain organization of *Pf*PKG, including a regulatory region with four CBDs and a C-terminal catalytic kinase domain. CBD-C is degenerate and does not bind cGMP. *B*, structures of *apo* (*red*) and cGMP-bound (*green*) CBD-D (*Pf*D). The invariant β-subdomain is *gray* in both structures. *C*, cGMP-binding pocket of *Pf*D and selected cGMP-interacting residues. *Black dashed lines*, hydrogen bonds. *Red dashed line*, hydrophobic interaction. *D*, similar to *B* but with 180° vertical rotation, highlighting the Tyr[480]–Arg[528] interaction. *E*, four-state thermodynamic equilibrium of the essential regulatory CBD (*i.e.* *Pf*D). The *apo* *Pf*D samples an autoinhibitory equilibrium between inactive and active states, which is coupled to the cGMP-binding equilibrium. *F* and *G*, hypotheses to explain *Pf*PKG inhibition, as reversal of a two-state equilibrium (*F*) or stabilization of an intermediate with mixed active and inactive features and diminished activation competency (*G*). *H–K*, base-substituted cGMP analogs investigated here. *L*, maximum *Pf*PKG kinase activities induced by cGMP and the cGMP analogs in *I–K*. Error bars represent the S.D.

pervasiveness of the effects caused by the cGMP modification (Fig. 3, *A* and *C–E*) also reflects the extent of inhibition. The perturbations resulting from the replacement of cGMP with either 8-NBD-cGMP or 8-pCPT-cGMP extend throughout the *Pf*D structure, whereas the least inhibitory analog, PET-cGMP,

perturbs only a relatively limited region near the cGMP-binding pocket (Fig. 3, *A* and *C–E*).

Overall, the data of Fig. 3 suggest that chemical shifts are ideally suited to investigate the dynamical allosteric transitions underlying *Pf*PKG inhibition. This notion is fully consistent
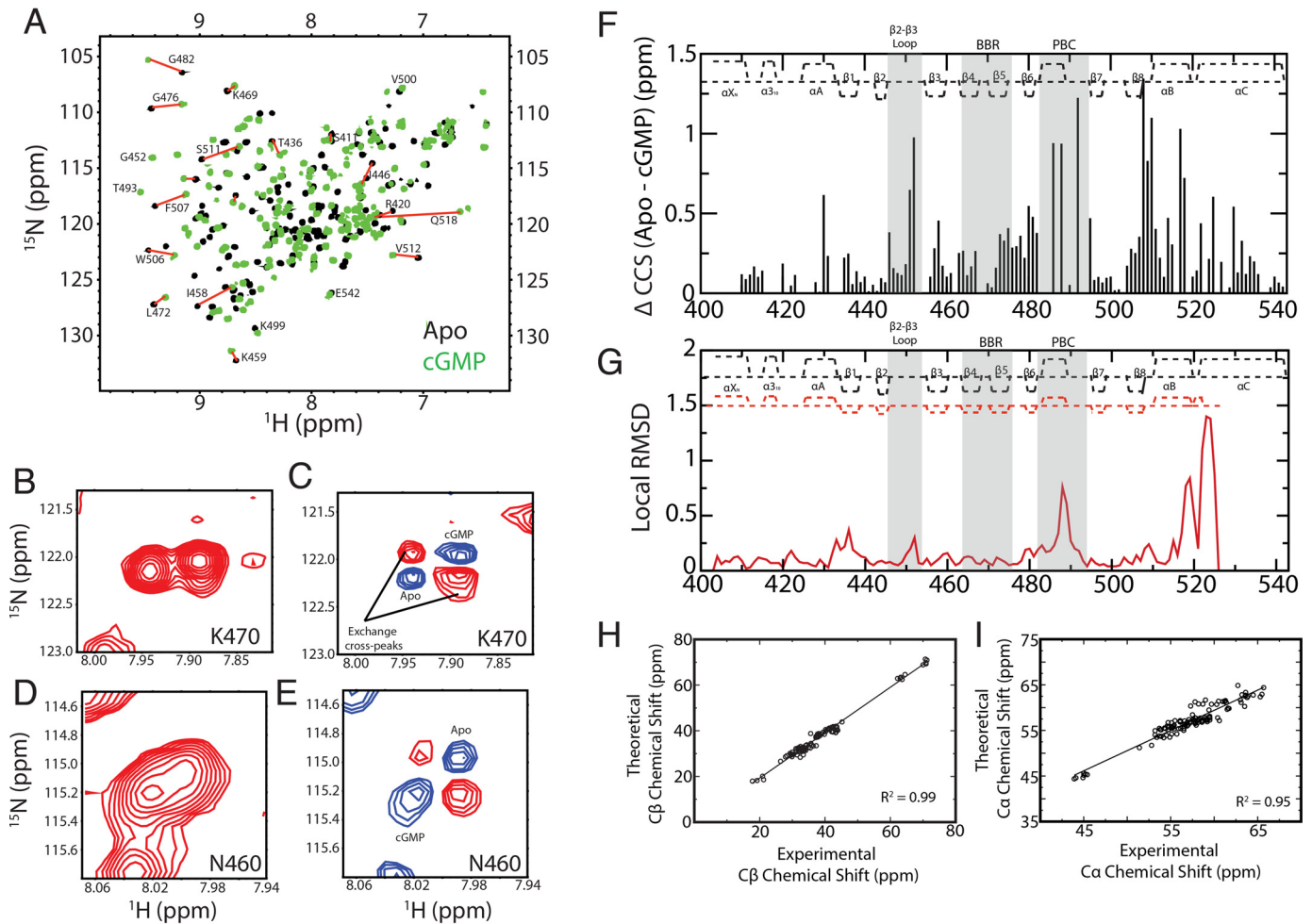
Figure 2. The *apo versus* cGMP-bound comparative NMR analyses of *Pf*D reveal pervasive allosteric perturbations. *A*, overlay of ^{15}N-^{1}H HSQC spectra of *apo* (*black*) and cGMP-bound (*green*) *Pf*D samples with representative assignments. N_z-exchange (*B* and *D*) and N_z-exchange difference experiments (*C* and *E*) utilized to transfer the assignments from the cGMP-bound to the *apo* spectra. *F*, CCS differences between the *apo* and cGMP-bound samples. The secondary structure of *Pf*D is depicted at the *top* of the *plot*. The cGMP-binding regions BBR and PBC as well as the adjacent β2–3 loop are *highlighted* in *gray background*. *G*, local *apo* (PDB code 4OFF) *versus* cGMP-bound (PDB code 4OFG) root mean square deviation for *Pf*D. The secondary structures obtained from the *apo* and cGMP-bound crystals are reported as *red* and *black dashed lines*, respectively. *H*, Cβ chemical shift values of cGMP-bound *Pf*D obtained from NMR triple-resonance experiments *versus* the theoretical Cβ chemical shift values predicted form the structure (PDB code 4OFG) using the ShiftX software (54). *I*, similar to *H* but for the Cα chemical shifts.

with the fast exchange between the inactive and the active states of CBDs (27–33), whereby the observed NMR peak positions are population-weighted averages of the pure inactive and active ppm values. Hence, chemical shifts report on the position of the dynamic inactive-active CBD conformational equilibrium. Chemical shift projection analysis (CHESPA) is an effective means to evaluate the perturbation of such dynamic equilibria caused by ligand modifications (28, 29, 31, 32). In the CHESPA analysis, the NMR peak positions of the cGMP analog–bound sample are evaluated relative to a reference vector connecting the peaks of the *apo*-inactive and the cGMP-bound active samples (Fig. 4, *A* and *D*). Specifically, the angle (θ) arising from the cGMP analog–bound *versus* cGMP-bound vector relative to the reference vector and the normalized projections onto the reference vector (*i.e.* fractional shift, X) are quantified through CHESPA (Fig. 4, *A* and *D*). The cos(θ) values report on the direction of the cGMP analog–induced shifts, whereas the X values gauge the extent of such shift toward inhibition or activation.

CHESPA of the cGMP analog– bound PfDs reveals the presence of a third "mixed" conformer with an engaged pre-lid but a disengaged lid

The CHESPA of 8-NBD-cGMP shows that the majority of residues exhibit negative X values (Fig. 4B), suggestive of most residues shifting toward the inactive state upon binding of 8-NBD-cGMP. However, the magnitudes of the X values are highly residue-dependent, pointing to deviations from the pure inactive-active two-state equilibrium, which predicts similar X values for residues outside the binding site. Another characteristic of a two-state model is the co-linearity of the perturbation and reference vectors (*i.e.* |cos(θ)| ∼ 1) for residues outside the binding site. However, the CHESPA of 8-NBD-cGMP reveals that several residues not in the binding site exhibit |cos(θ)| values significantly less than 1 (Fig. 4C), suggesting deviations from the two-state model and pointing to the presence of additional state(s) sampled by the *Pf*D: 8-NBD-cGMP complex. Similar trends are observed for the 8-pCPT-cGMP–bound sample (Fig. 4, *E* and *F*).
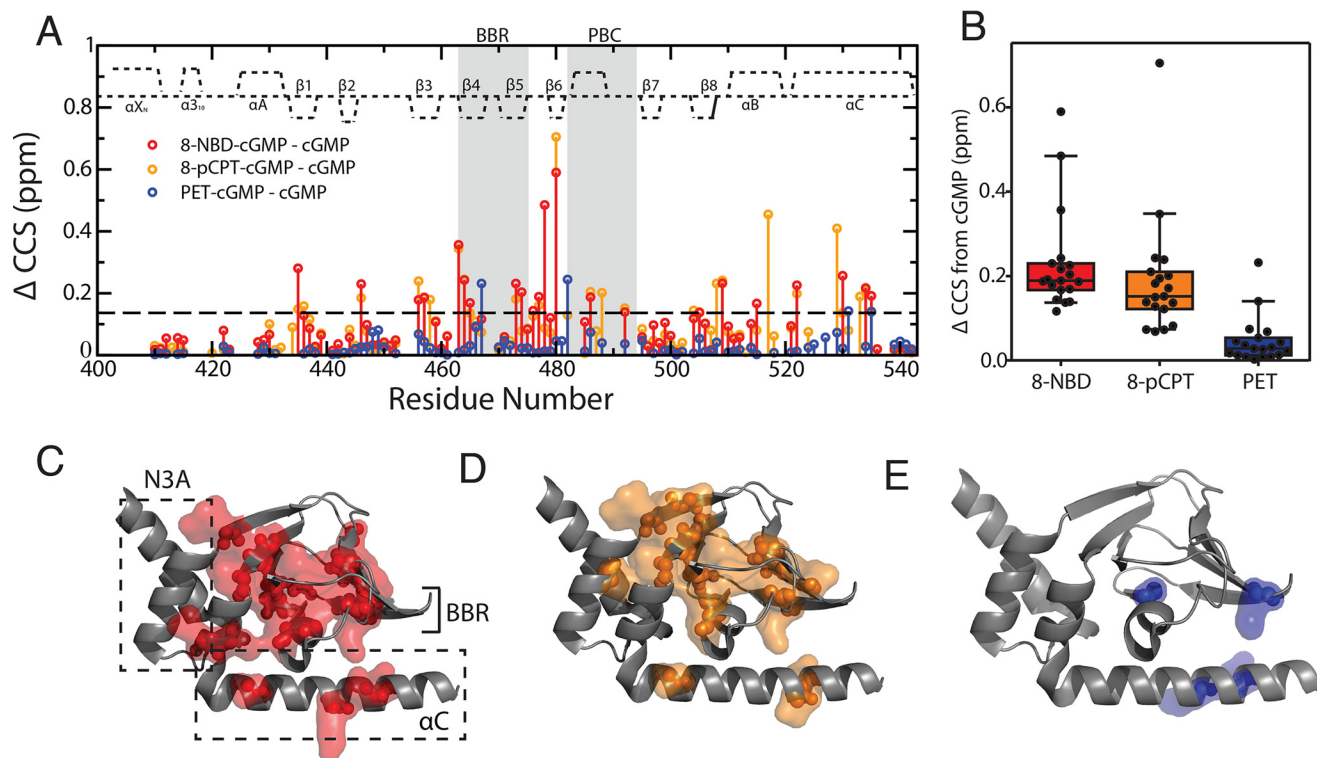
Figure 3. cGMP analog *versus* cGMP chemical shift differences report on inhibitory conformational changes of *Pf*D. *A*, ΔCCS between cGMP and 8-pCPT-cGMP (*orange*), 8-NBD-cGMP (*red*), and PET-cGMP (*blue*) bound *Pf*D plotted against residue numbers. *Dashed line*, average ΔCCS + 2 S.D. of PET-cGMP. *B*, box plot (10–90% percentile) of ΔCCS differences between cGMP-bound and the 8-NBD-cGMP–, 8-pCPT-cGMP–, and PET-cGMP– bound samples. Residues included in the box plot correspond to residues that are assigned in all samples and with at least one of the three ΔCCS > average + 2 S.D. of PET-cGMP (*dashed line in A*). *C–E*, residues with CCS changes greater than the *dashed line* in *A* mapped onto the active structure of *Pf*D for the 8-NBD-cGMP (*C*), 8-pCPT-cGMP (*D*), and PET-cGMP (*E*) bound samples. *Error bars*, S.D.

The presence of multiple conformational equilibria is further supported by the width of the X value distributions (Fig. 4*G*). The X distributions measured for 8-NBD-cGMP– and 8-pCPT-cGMP– bound *Pf*D are significantly wider compared with PET-cGMP (Fig. 4*G*), which is nearly a full agonist and samples mainly the active state (Fig. S2). These observations suggest that the *Pf*D:8-NBD-cGMP and *Pf*D:8-pCPT-cGMP complexes sample a multistate ensemble, including not only the inactive and active conformers represented by the *apo* and cGMP-bound crystal structures, but also an additional state or states.

To simplify the analysis, we focused on the C-terminal helices that are directly linked to the catalytic domain and are one of the allosteric elements most critical in the inhibition and activation of the kinase (14, 21, 24). The C-terminal helices span two regions with clearly distinct average X values ($\langle X \rangle$) in the *Pf*D:8-NBD-cGMP complex: residues 515–530, denoted as the pre-lid with $\langle X \rangle = -0.48$, and residues 534–535, denoted as the lid with $\langle X \rangle = -0.88$ (Fig. 4, *B*, *H*, and *I*). This means that for the *Pf*D:8-NBD-cGMP complex, the pre-lid only shifts about halfway toward the inactive state, whereas the lid region shifts almost completely to the inactive state. A similar trend is observed for the *Pf*D:8-pCPT-cGMP complex with average X values of -0.30 and -0.64 in the pre-lid and the lid regions, respectively.

One of the simplest models to explain both the enzymatic and the NMR data in Figs. 1*L* and 4, respectively, is a three-state equilibrium mechanism involving an inactive, an active, and an

intermediate state (Fig. 5*A*). The inactive state is similar to the *apo-Pf*D structure, where both the pre-lid and the lid are disengaged. The active state is similar to the cGMP-bound structure, where both the pre-lid and the lid are engaged. The intermediate state exhibits a mixed character, as the pre-lid is engaged similarly to the active state, but the lid is disengaged, similarly to the inactive state (Fig. 5*A*). Next, we checked whether it is possible to utilize this three-state model to back-calculate the relative kinase activities.

The CHESPA-based three-state model of PfD inhibition explains the experimental kinase activities

Using the average X values for the pre-lid and the lid regions (Fig. 4, *B* and *E*) and Fig. S2*A*), the populations of the inactive, intermediate, and active states were estimated. Because the pre-lid is disengaged only in the inactive state, the average X of the pre-lid reflects the population of the inactive state. Similarly, the lid is engaged only in the active state. Hence, the population of the active state is estimated as $1 - \langle X \rangle_{\text{lid}}$. The population of the intermediate is the percentage not accounted for by the other two states. Using this approach, the populations of the inactive, intermediate, and active states for the *Pf*D:8-NBD-cGMP complex are 48 ± 12, 40 ± 12, and $12 \pm 1\%$, respectively (Fig. 5*A* and Table S1). Similarly, the three state populations can be calculated for the 8-pCPT-cGMP– and PET-cGMP– bound *Pf*D complexes based on the respective CHESPA data (Fig. 4*E*, Fig. S2, and Table S1). Using these populations and assuming that the inactive and intermediate states are fully inhibitory,
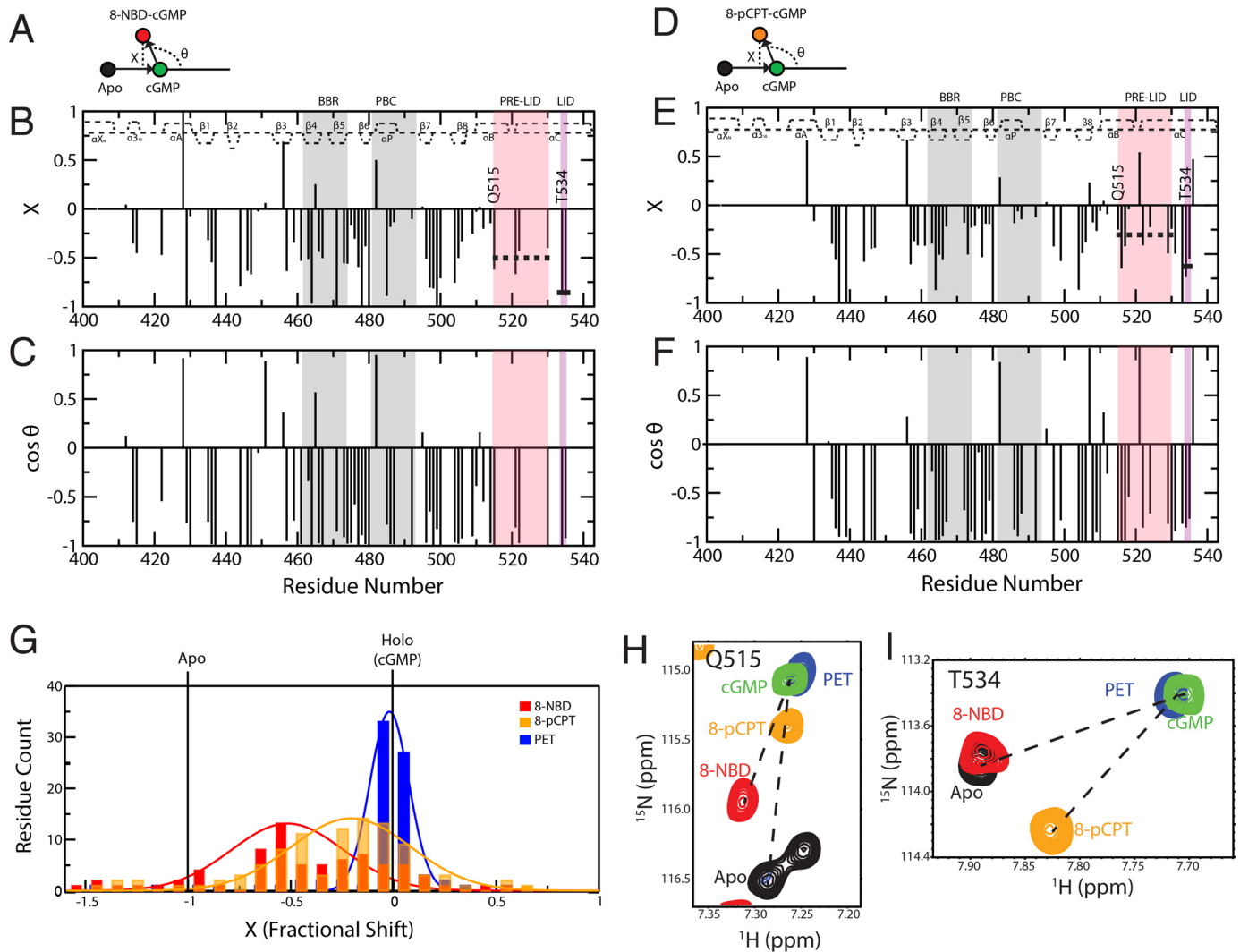
Figure 4. CHESPA of cGMP analog–bound states reveals a third conformer with a disengaged lid. CHESPA vector scheme, fractional shift (*X*) and cos(*θ*) values plotted against residue number for 8-NBD-cGMP (*A–C*) and for 8-pCPT-cGMP (*D–F*). The secondary structure of cGMP-bound *Pf*D is depicted at the *top* of each plot. Pre-lid and lid motifs are *highlighted* in *pink* and *purple background*, respectively. The PBC and BBR are *highlighted* in *gray background*. The average ⟨*X*⟩ values for residues common in both 8-NBD-cGMP–bound and 8-pCPT-cGMP–bound sample are indicated with a *dashed* and a *solid line* for the pre-lid and the lid motifs, respectively. *G*, distribution of *X* values for 8-NBD–, 8-pCPT–, and PET-cGMP–bound samples. *H* and *I*, HSQC overlay expansions for representative residues in the pre-lid and lid regions of the *apo* (*black*) and the 8-NBD-cGMP (*red*), 8-pCPT-cGMP (*orange*), PET-cGMP (*blue*), and cGMP (*green*) bound samples.

given the lid disengagement (14), while the active state is non-inhibitory, the relative kinase activity at ligand saturation induced by these cGMP analogs was predicted. The predicted activation values correlate well with the experimental kinase activity values (Fig. 5*B*).

The ability of our three-state model to recapitulate the enzymatic data has three key implications. First, the measurements on the *Pf*D construct are relevant for the longer *Pf*PKG construct used in the kinase assays to probe the *Pf*PKG function. Second, the NMR chemical shift projection analysis and the resulting fractional shift values are suitable for predicting the populations of different functional states. Third, the mixed intermediate state, where only the lid region is disengaged, is inhibitory to an extent similar to the inactive state, further corroborating the pivotal role of the lid region in activation. Hence, we further probed the inhibitory mixed intermediate stabilized by the 8-NBD-cGMP analog.

8-NBD-cGMP binds to PfD in a syn conformation and perturbs interactions critical for activation

As a first step toward investigating the mixed intermediate, we examined the base orientation of 8-NBD-cGMP as bound to *Pf*D. Typically, the base of cyclic nucleotides is oriented either in *syn* or *anti* relative to the ribose ring (34–38). To determine whether the guanine base of 8-NBD-cGMP is *syn* or *anti*, we could not rely on NOE-based assessments, as this cGMP analog lacks nonexchangeable protons in the base. Hence, we focused on the chemical shifts of the Cγ^2 methyl of Ile[465], which in the *Pf*D:cGMP complex is in direct contact with the guanine base, and of the Cγ methyl of Thr[493], whose hydroxyl interacts with the amino group of cGMP (Fig. 1*C*). The chemical shifts of both Ile[465] Cγ^2 and Thr[493] Cγ show only marginal changes when cGMP is replaced by 8-NBD-cGMP (Fig. 6, *A* and *B*), suggesting that the 8-NBD-cGMP guanine base binds in a *syn* conformation, similar to cGMP. This conclusion was confirmed also by
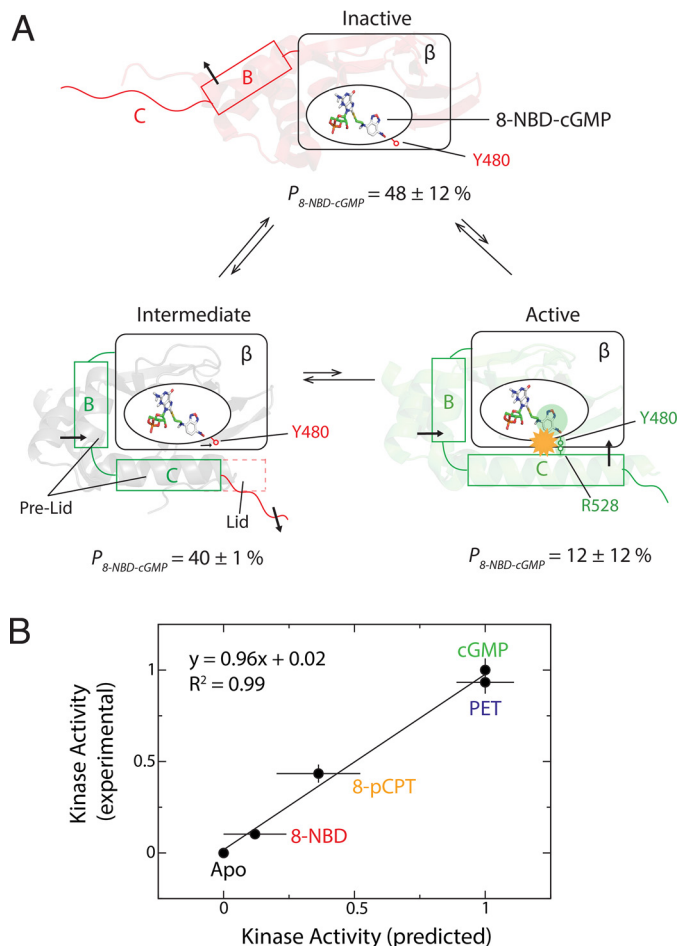
Figure 5. Proposed model for PfD inhibition by 8-NBD-cGMP and comparison of calculated *versus* measured kinase activities. *A*, inhibition occurs through a three-state equilibrium, sampling a distinct *holo*-inactive intermediate state, where the pre-lid and PBC are engaged, similarly to the active state, but the lid is disengaged, similarly to the inactive state. The population of each state (*P*) is indicated. The structural shifts of the αB and αC helices are indicated with *black arrows*. The β-barrel is indicated with a *rectangular box*. The *yellow starburst* indicates the steric clash between the 8-NBD substituent and the Arg528 side chain. *B*, correlation plot of experimental *versus* predicted relative kinase activities. The kinase activity prediction is based on the populations of inactive, intermediate, and active states (Table S1). *Error bars* for the experimental kinase activity represent the standard deviation of multiple measurements, and for the predicted kinase activity represent the errors propagated from the errors on the populations, which are determined from the standard deviation of the fractional shift (*X*) values of the residues used to calculate the average *X* values.

the 3D map of 8-NBD-cGMP *versus* cGMP NH CCS changes for residues in the β-barrel (Fig. 6C, *red surface*). Because residues in the β-barrel do not undergo significant structural changes upon cNMP binding, the perturbations sensed by the ΔCCS report mainly on direct binding contacts (33, 39–41). The ΔCCS map is fully consistent with 8-NBD-cGMP binding in *syn* rather than *anti* guanine orientation (Fig. 6C, residues within the *red surface*). Similarly, we confirmed through the β-barrel ΔCCS map that a *syn* orientation is preserved also for the guanine base of PET-cGMP (Fig. 6D, *blue surface*). For this analog, the substitution is at the 1- and 2- rather than the 8-position (Fig. 1, *I* and *K*), causing the most significant CCS changes to cluster at the opposite side of the β-barrel for PET-cGMP compared with 8-NBD-cGMP, when both analogs maintain a

syn guanine orientation (Fig. 6, *C* and *D*, *blue versus red surfaces*).

Although 8-NBD-cGMP preserves a *syn* guanine orientation when bound to PfD, similar to cGMP, the introduction of the 8-NBD moiety has a profound effect on the conformational ensemble accessed by PfD, as shown by the NMR-based three-state model of Fig. 5A. Of the three PfD conformers in Fig. 5A, the mixed intermediate is the least characterized. Hence, we utilized MD simulation to further investigate this intermediate. For this purpose, we built a hybrid structure to resemble the intermediate state proposed based on the CHESPA data (Fig. 5A), relying on the cGMP-bound coordinates (PDB code 4OGF) (14) for residues 401–532 and on the *apo* coordinates (PDB code 5DYK) (24) for residues 534–542, which span the lid region. The hybrid model provided the initial coordinates for a 1-μs MD trajectory, and Fig. 6 (*E* and *F*) shows representative structures selected based on the cluster analysis of such trajectory (Table S2).

In agreement with the data of Fig. 6 (*A*–*C*), Fig. 6E shows that the PfD-bound 8-NBD-cGMP preserves a *syn* guanine orientation. Fig. 6F illustrates that the lid region of the intermediate state is disengaged, whereas the pre-lid is engaged. Fig. 6G shows that when the intermediate conformation is overlaid with the cGMP-bound structure (PDB code 4OFG), the Arg528 side chain of 4OFG clashes with the NBD moiety of 8-NBD-cGMP (Fig. 6G, *gray sticks*). The steric clash explains why in the simulated intermediate structure, the Arg528 side chain moves away from the 8-NBD-cGMP and rotates outward, breaking the interaction with Tyr480 (Fig. 6G, *red sticks*). Considering that the Tyr480–Arg528 interaction is critical for activation (14, 21), the perturbation of Arg528 caused by 8-NBD is consistent with the lack of kinase activity observed upon replacement of cGMP with 8-NBD-cGMP.

This perturbation revealed by the MD simulations is consistent with the significant 8-NBD-cGMP *versus* cGMP chemical shift changes occurring at or near Tyr480 (Fig. 3A). The Tyr480 NH HSQC cross-peak of the cGMP:PfD complex moves completely toward the *apo* position when cGMP is replaced by 8-NBD-cGMP (Fig. 6H), confirming that the 8-NBD moiety perturbs the Tyr480–Arg528 interaction. To further corroborate this result, we generated the R528K mutant and compared the R528K *versus* WT chemical shifts for both cGMP– and 8-NBD-cGMP–bound samples (Fig. 6I). For the cGMP:PfD complex, the largest R528K *versus* WT ΔCCS values cluster primarily close to Tyr480 (Fig. 6I), as expected based on the Arg528–Tyr480 interaction observed in the cGMP:PfD structure (14). However, when cGMP is replaced by 8-NBD-cGMP, the R528K *versus* WT CCS changes in the vicinity of Tyr480 are markedly suppressed (Fig. 6I), confirming that in the 8-NBD-cGMP:PfD complex, the Arg528–Tyr480 interaction is significantly weakened compared with the cGMP:PfD structure.

Similar analyses were carried out to probe the effect of 8-NBD-cGMP on the capping triad interactions between Arg484, Gln532, and Asp533, which are also critical for activation (14). We found that the Arg484–Asp533 interaction is perturbed in the simulated intermediate structure of the 8-NBD-cGMP:PfD complex (Fig. S3A). To confirm such perturbation, we measured the CCS changes between WT and the R484A mutant for
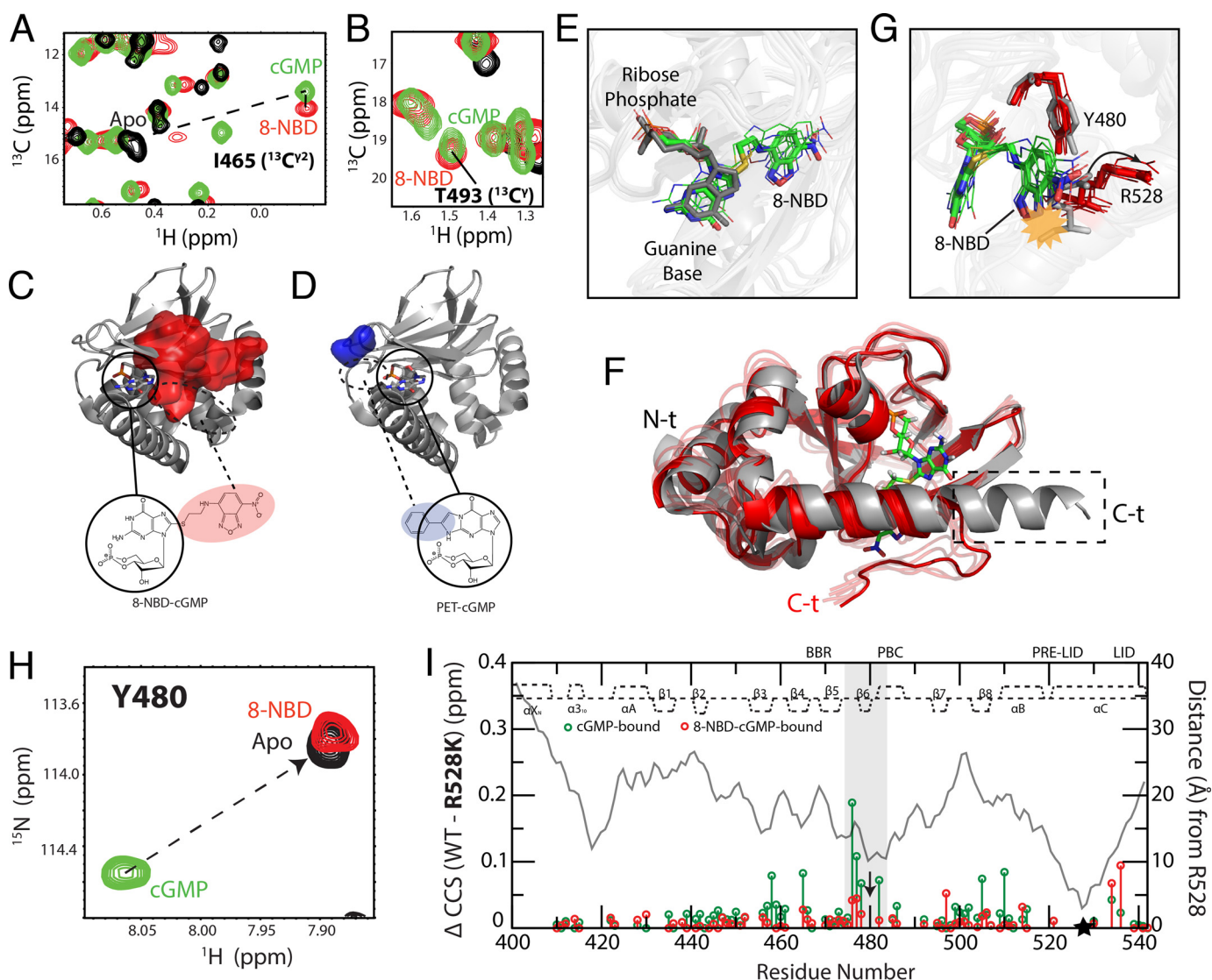
Figure 6. Syn conformation of 8-NBD-cGMP bound to *Pf*D and effect of 8-NBD on the Tyr[480]–Arg[528] interaction. *A* and *B*, overlaid ¹³C-¹H HSQC spectral expansions of *apo* (*black*), cGMP-bound (*green*), and 8-NBD-cGMP– bound (*red*) *Pf*D, zoomed into Ile[465] (¹³C²) (*A*) and Thr[493] (¹³Cᵞ) (*B*), which interact with the guanine base of cGMP. The *apo* peak for Thr[493] (¹³Cᵞ) could not be assigned. *C* and *D*, map of residues in the β-barrel that exhibit ΔCCS relative to cGMP-bound *Pf*D greater than the average ΔCCS + 2 S.D. of the PET-cGMP *versus* cGMP ΔCCS for the 8-NBD-cGMP-bound (*C*) and PET-cGMP– bound (*D*) *Pf*D. *Circles* indicate the cGMP portion of the analog in its *syn* orientation (PDB code 4OFG). The *dashed circles* represent the region where the base substituents (*i.e.* 8-NBD or PET) are expected to be located when the cGMP portion of the analogs is in the *syn* orientation. *E*, overlay of the structure of cGMP:*Pf*D (PDB code 4OFG) and representative structures of 8-NBD-cGMP:*Pf*D generated from MD simulations (Table S2). The cGMP (*dark gray*) aligns with the cGMP portion of the 8-NBD-cGMP (*green*, carbon; *white*, hydrogen; *blue*, nitrogen; *red*, oxygen; *yellow*, sulfur; *orange*, phosphorus). *F*, aligned representative structures of 4OFG (*gray*) and 8-NBD-cGMP:*Pf*D (*red*) generated from MD simulations. The *dashed box* indicates the portion of the C-terminal αC helix that becomes disordered in the 8-NBD-cGMP:*Pf*D intermediate. *G*, similar to *F*, but zoomed into the Tyr[480]–Arg[528] region. The *yellow starburst* indicates the steric clash of 8-NBD moiety with the Arg[528] side chain in the 4OFG structure. The *arrow* indicates the structural shift of the Arg[528] side chain upon binding of 8-NBD-cGMP. *H*, ¹H-¹⁵N HSQC spectra of *apo* (*black*), cGMP-bound (*green*), and 8-NBD-cGMP-bound (*red*) samples overlaid and zoomed in on Tyr[480]. *I*, WT *versus* R528K CCS differences for cGMP-bound (*green*) and 8-NBD-cGMP– bound (*red*) samples. Residues assigned in both the cGMP-bound and the 8-NBD-cGMP– bound samples are plotted. The distance (Å) measured from Arg[528] using the cGMP-bound structure (PDB code 4OFG) is shown in a *gray line*. The secondary structure of cGMP-bound *Pf*D is depicted at the *top* of each plot. The *highlighted region* indicates residues near Tyr[480], where the perturbation induced by the R528K mutation in the cGMP-bound complex is lost when cGMP is replaced by 8-NBD-cGMP. *Black arrow*, Tyr[480]; *black star*, Arg[528].

both the cGMP– and 8-NBD-cGMP– bound samples (Fig. S3*B*). Fig. S3*B* reveals that the R484A *versus* WT CCS changes in the C-terminal helices, especially in the vicinity of Gln[532]–Asp[533], are suppressed when cGMP is replaced with 8-NBD-cGMP, confirming that 8-NBD-cGMP perturbs the capping interaction between Arg[484] and the C-terminal helices. These results are in full agreement with the MD simulations, suggesting that the 8-NBD substituent destabilizes also the capping triad.

Hence, we conclude that upon introduction of the NBD group at the 8-guanine position, the *syn* base orientation is pre-

served but the Tyr[480]–Arg[528] contact and the capping triad interactions are significantly perturbed, thus compromising the full engagement of the C-helix and explaining why 8-NBD-cGMP functions as an effective allosteric antagonist of the *Pf*PKG kinase.

Sampling a mixed intermediate state is beneficial for maximizing kinase inhibition while minimizing affinity losses

The three-state model with the mixed intermediate state featuring an engaged pre-lid and a disengaged lid (Fig. 5*A*) pro-
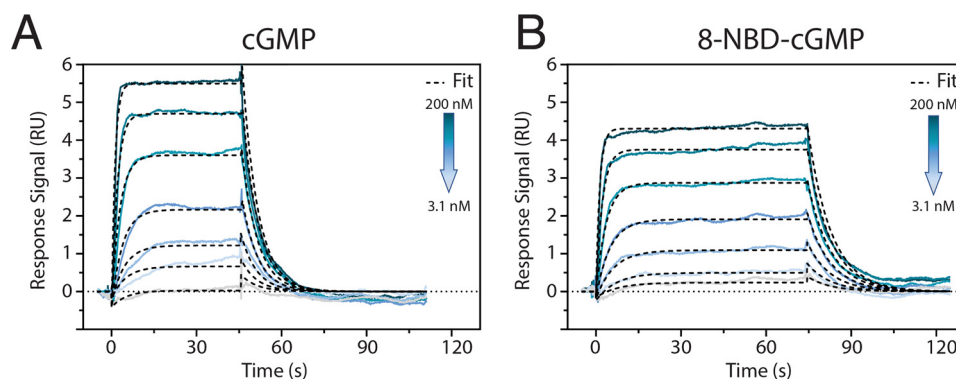
Figure 7. Surface plasmon resonance binding studies of cGMP and 8-NBD-cGMP to *Pf*PKG 401–853 (*Pf*D-catalytic domain) demonstrate similar binding kinetics. Direct binding assays were performed by capturing polyhistidine-tagged *Pf*PKG 401–853 on a Ni-NTA sensor chip and injecting a dilution series of cGMP for 45 s (*A*) and 8-NBD-cGMP for 70 s (*B*), respectively. Rate and equilibrium binding constants are reported in Table S3. A Langmuir 1:1 model was applied for fitting.

vides an excellent strategy for *Pf*PKG kinase inhibition without significantly compromising affinity. Reconciling high inhibitory efficacy and potency would be more challenging for a simple two-state model. In this case, the disengagement of the lid necessary for inhibition also implies the concurrent disengagement of other *Pf*D elements necessary for high-affinity binding, such as the PBC in its entirety. On the contrary, in the mixed intermediate state (Fig. 5*A*), which exhibits an inhibitory effect similar to that of the inactive state, it maintains the pre-lid and the adjacent PBC engaged. For example, whereas the capping carboxylate of Asp[533] is displaced away from Arg[484] in the PBC, the side chain of this arginine in the mixed intermediate remains in an orientation similar to the active conformation (Fig. S3*A*), thus minimizing perturbations of the interactions with the cyclic nucleotide. Hence, based on the three-state model of Fig. 5*A*, we hypothesize that the 8-NBD-cGMP preserves an affinity comparable with the endogenous allosteric effector, cGMP.

Our hypothesis is confirmed through surface plasmon resonance (SPR) measurements (Fig. 7) showing that the affinities of 8-NBD-cGMP and cGMP are comparable (*i.e. K_d* = 59 ± 4 nM *versus* 51 ± 7 nM; Table S3), despite their markedly different efficacies in terms of kinase activation (Fig. 1*L* and Fig. S1*A*). This conservation of affinity is especially important, because 8-NBD-cGMP acts as a competitive antagonist (Fig. S1*B*). Hence, 8-NBD-cGMP serves as an excellent example for how sampling a mixed intermediate state enables significant inhibition without major affinity losses by selectively disengaging only structural units strictly necessary for kinase activation. Similar inhibition strategies are anticipated to inform the design of future *Pf*PKG allosteric inhibitors, which may serve as anti-malaria drug leads.

Experimental procedures

Expression and purification

The *Pf*PKG CBD-D construct (residues 401–542) (*i.e. Pf*D) within a His-tagged expression vector pQTEV (14) was expressed in the *Escherichia coli* strain BL21 (DE3). The transformed *E. coli* was grown in a minimal medium enriched with $^{15}NH_4Cl$ and [^{13}C]glucose and supplemented with D-biotin, thiamine HCl, $MgSO_4$, and $CaCl_2$. The cells were grown at

37 °C to an optical density of 0.7 (at λ = 600 nm), induced with 0.5 mM isopropyl 1-thio-β-D-galactopyranoside, and then incubated for an additional 18 h at 18 °C. Cells were harvested, resuspended in the lysis buffer (50 mM Tris, pH 7.4, 500 mM NaCl, 1 mM BME), and lysed using a cell disruptor. The cell debris was removed through centrifugation, and then the supernatant was loaded onto an Ni^{2+}-Sepharose resin. The cell lysate was allowed to flow through, and the column was rinsed with 50 mM Tris, pH 7.4, 500 mM NaCl, 1 mM BME, and 20 mM imidazole. After thorough rinsing, the protein was eluted with 50 mM Tris, pH 7.4, 500 mM NaCl, 1 mM BME, and 300 mM imidazole. The eluted protein was then dialyzed in 50 mM Tris, pH 7.4, 100 mM NaCl, 1 mM BME with tobacco etch virus protease for 24 h at 4 °C. The cleaved products were loaded on the Ni^{2+}-Sepharose resin. The protein without the His-tag was obtained through collecting the flow-through and was further purified with a HiLoad 16/60 Superdex 75 gel filtration column (GE Healthcare) equilibrated with NMR buffer (50 mM Tris, pH 7, 100 mM NaCl, 10 mM $MgCl_2$, 1 mM DTT). The His-tagged *Pf*PKG 401–853 construct including the catalytic domain was expressed in *E. coli* TP2000 and purified using Ni-NTA and size-exclusion chromatography, as described previously (21).

NMR spectroscopy

NMR experiments were performed on a Bruker Avance 700-MHz spectrometer equipped with a 5-mm TCI cryoprobe or a Bruker Avance 850-MHz spectrometer equipped with a triple-resonance TXI probe. All experiments were acquired at 306 K in NMR buffer (50 mM Tris, pH 7, 100 mM NaCl, 10 mM $MgCl_2$, 1 mM DTT) with 5% D_2O. All NMR spectra were processed with NMRPipe (42) and analyzed using Sparky (43). Three-dimensional triple-resonance NMR experiments (*i.e.* HNCACB, CBCA(CO)NH, HNCA, HN(CO)CA, HNCO, HCCH-TOCSY, and (H)CC(CO)NH) were acquired and used to assign the two-dimensional ^1H-^{15}N HSQC and ^1H-^{13}C HSQC NMR spectra of cGMP-bound *Pf*D. Because the *apo* sample was prone to precipitation, 2D N_z-exchange, 2D difference N_z-exchange, and 2D C_z-exchange experiments with mixing time of 250 ms were used to transfer the chemical shift assignments from the cGMP-bound *Pf*D to the *apo*-*Pf*D spectra. The cGMP analog–bound spectra were assigned through spectral comparison with

cGMP-bound spectra, if no ambiguities were present, and through 2D N_z exchange and 2D difference N_z exchange with the *apo* state. Chemical shift assignments of R528K:cGMP and R528K:8-NBD-cGMP were obtained through spectral comparison with WT spectra if no ambiguities were present.

Chemical shift analyses

All spectra utilized for chemical shift analyses were acquired with 100 μM *Pf*D and saturating amounts of cGMP or cGMP analogs (2 mM) or without any cNMP addition for *apo* spectra. For accurate chemical shift comparisons, an internal reference (*i.e.* ^{15}N-labeled *N*-acetylglycine) was used to align the spectra in Sparky, and the resulting chemical shift values were used to compute the compounded chemical shift differences and perform CHESPA following protocols described previously (29, 30, 34, 44, 45). The fractional shift (X) values and cos(θ) values were computed for residues with cGMP analog–bound *versus* cGMP-bound CCS difference >0.05 ppm. The average ⟨X⟩ values for the pre-lid and the lid were calculated using residues that were assigned in all five samples (*i.e. apo*, cGMP-bound, 8-NBD-cGMP-bound, 8-pCPT-cGMP-bound, and PET-cGMP-bound *Pf*D), had X values between 0 and -1, and had ΔCCS (cGMP analog–bound *versus* cGMP-bound) values greater than 0.05 ppm, ensuring reliable X and cos(θ) values. The distribution of X values for cGMP analogs was computed using the residues that exhibited $|\cos(\theta)| > 0.75$ to minimize biases from nearest-neighbor effects.

Site-directed mutagenesis

The R528K mutation was created through site-directed mutagenesis using a KOD Hot Start Master mix (Novagen) and primer pairs (synthesized by IDT): forward, CTGGCCCACTTGGAAGAGAAGATTAAGATGCAGGATAC; reverse, GTATCCTGCATCTTAATCTTCTCTTCCAAGTGGGCCAG. The reaction protocol provided by the KOD Hot Start kit was followed. Template DNA was degraded with DpnI for 2 h at 37 °C, and the reaction product was used for transformation of *E. coli* top10 cells. The transformed colony was grown in lysogeny broth or Luria-Bertani medium medium for 18 h at 37 °C. Plasmids were isolated from the *E. coli* using the GeneJET Plasmid Miniprep Kit (Thermo Fisher Scientific). The purified plasmids were sequenced to verify the mutation. The expression and purification of *Pf*D R528K were carried out using the same protocol as for the WT *Pf*D.

Kinase assays

Specific kinase activities were determined using an enzyme-coupled spectrophotometric assay (46). In a quartz cuvette, purified *Pf*PKG 401–853 was mixed with the reaction buffer (100 mM MOPS, pH 7.0, 10 mM MgCl$_2$, 5 mM β-mercaptoethanol, 1 mM ATP, 1 mM phosphoenolpyruvate, 230 μM NADH, 15 units/ml lactate dehydrogenase, 8.4 units/ml pyruvate kinase). The reactions were started by adding 1 mM PKStide (GRTGRRNSI; GeneCust, Luxembourg) and monitored in the absence and presence of a 100 μM concentration of each cyclic nucleotide (cGMP, 8-pCPT-cGMP, and PET-cGMP) for at least 1 min. Specific kinase activity was calculated according to the Lambert–Beer law.

Kinase activity induced by 8-NBD-cGMP was measured by microfluidic mobility shift assay using a Caliper DeskTop Profiler (PerkinElmer Life Sciences). Here, 100 μM cGMP or 8-NBD-cGMP was mixed with assay buffer (20 mM MOPS (pH 7), 300 mM NaCl, 10 mM MgCl$_2$, 1 mM ATP, 1 mM DTT, 990 μM PKStide, 10 μM FITC-PKStide (FITC-GRTGRRNSI; GeneCust, Luxembourg, 0.05% L-31) and a fixed protein concentration and continued as described previously (21). The assay was also conducted with multiple concentrations of 8-NBD-cGMP or cGMP, ranging from 0.1 nM to 300 μM. For the competition assay, the protein was preincubated with 350 nM cGMP, varying concentrations of 8-NBD-cGMP were added to the reaction, and substrate conversion was monitored over 2 h. The combined kinase inhibition data were further analyzed and normalized using GraphPad Prism 8.3.0 (GraphPad Software).

SPR

Direct binding data were obtained via SPR using a Biacore T200 (GE Healthcare Life Sciences). Briefly, 200–300 RU of Ni^{2+} (5 mM NiCl$_2$ in running buffer) were immobilized on a poly-NTA–derivatized sensor chip (NIHC 1000M; XanTec Bioanalytics GmbH). Subsequently, His-tagged *Pf*PKG 401–853 in running buffer (20 mM HEPES, 150 mM NaCl, 50 μM EDTA, 0.01% P20, pH 7.3) was captured at a flow rate of 10 μl/min to an immobilization level of 500–2500 RU. Next, association was measured by injection of a dilution series of the respective cyclic nucleotide for 45–75 s. Then running buffer was injected for 60–180 s to initiate dissociation. Regeneration of the sensor chip surface was achieved by consecutively injecting 0.5 M EDTA (pH 8) for 600 s, followed by injections of 3 M guanidinium HCl, 0.5% SDS, and 3 M guanidinium HCl for 240 s each. Unless stated otherwise, all kinetic measurements were performed at 25 °C in running buffer and a flow rate of 50 μl/min. Data were evaluated with the Biacore T200 Evaluation Software 3.0 using a global fit and assuming a 1:1 Langmuir binding model. Further data processing was performed using GraphPad Prism 8.3.0 (GraphPad Software).

Molecular dynamic simulations: initial model preparation

The structure of 8-NBD-cGMP in a *syn* conformation was generated using RDKit (47). A model of the mixed intermediate state sampled by the *Pf*D:8-NBD-cGMP complex was then built using residues 401–533 from the active *Pf*D:cGMP crystal structure (PDB code 4OFG) (14) and lid region residues 534–542 from the inactive *apo-Pf*D crystal structure (PDB code 5DYK) (24). The 8-NBD-cGMP ligand was docked into the resulting mixed structure of *Pf*D using AutoDock4 with default parameters generated by AutoDockTools (48). Residues 463–494, where the PBC and BBR regions are located, were assigned as the binding pocket for AutoDock. The structure in which the ribose-phosphate and guanine moieties of the docked ligand were best aligned with the position of cGMP in the cGMP-bound active structure (PDB code 4OFG) (14) was selected as the initial coordinates for MD simulations.

Molecular dynamics simulation protocol

All simulations were performed using the AMBER 16 software PMEMD.CUDA (49) on the Shared Hierarchical Aca-

demic Research Computing Network (SHARCNET). The Amber ff99SBnmr force field was employed for the protein, whereas RESP charge and the general Amber force field were applied to generate the parameters for 8-NBD-cGMP using the Gaussian09 program (50) and the antechamber module implemented in AMBER 16, as described previously (51). The TIP3P water model was applied in the form of a rectangular MD solvent box surrounding the *Pf*D:8-NBD-cGMP structure, with a minimum distance of 12 Å between the *Pf*D:8-NBD-cGMP structure and the box edge. To mimic the experimental conditions, the charged residues and N/C termini were set to the protonation states expected at pH 7, following a protocol similar to that implemented previously (52), and Na^+ and Cl^- ions were added to mimic a 100 mM salt concentration.

The simulations started with an energy minimization performed with harmonic restraints on the protein backbone (with a force constant of 5 kcal/mol·Å^2). The system was then gradually heated from 0 to 100 K at constant volume and then heated from 100 to 306 K in the NPT ensemble, and all of the heating process employed harmonic restraints on protein backbone (with a force constant of 3 kcal/mol·Å^2) for a total of 1 ns followed by an equilibration period of 1.2 ns with main-chain atoms restrained with a force constant of 1 kcal/mol·Å^2. Then a 1-μs production MD trajectory was generated in the NPT ensemble at 306 K and 1 atm with a weak-coupling algorithm, saving structures every 10 ps for subsequent analysis. A cluster analysis for 20,000 frames recorded from the MD trajectory (*i.e.* the structures recorded at 50-ps intervals) was performed, with β-core alignment, using the CPPTRAJ protocol (53).

Data availability

The NMR chemical shift assignment for cGMP-bound *Pf*D has been deposited in the Biological Magnetic Resonance Data Bank (BMRB) with the code 50203. All remaining data are contained within the article.

References

1. World Health Organization (2019) *World Malaria Report 2019*, World Health Organization, Geneva
2. Cowman, A. F., Healer, J., Marapana, D., and Marsh, K. (2016) Malaria: biology and disease. *Cell* **167,** 610–624 CrossRef Medline
3. Doerig, C., Billker, O., Pratt, D., and Endicott, J. (2005) Protein kinases as targets for antimalarial intervention: kinomics, structure-based design, transmission-blockade, and targeting host cell enzymes. *Biochim. Biophys. Acta* **1754,** 132–150 CrossRef Medline
4. Brochet, M., and Billker, O. (2016) Calcium signalling in malaria parasites. *Mol. Microbiol.* **100,** 397–408 CrossRef Medline
5. Hopp, C. S., Bowyer, P. W., and Baker, D. A. (2012) The role of cGMP signalling in regulating life cycle progression of *Plasmodium. Microbes Infect.* **14,** 831–837 CrossRef Medline
6. Taylor, H. M., McRobert, L., Grainger, M., Sicard, A., Dluzewski, A. R., Hopp, C. S., Holder, A. A., and Baker, D. A. (2010) The malaria parasite cyclic GMP-dependent protein kinase plays a central role in blood-stage schizogony. *Eukaryot. Cell* **9,** 37–45 CrossRef Medline
7. Moon, R. W., Taylor, C. J., Bex, C., Schepers, R., Goulding, D., Janse, C. J., Waters, A. P., Baker, D. A., and Billker, O. (2009) A cyclic GMP signalling module that regulates gliding motility in a malaria parasite. *PLoS Pathog.* **5,** e1000599 CrossRef Medline
8. McRobert, L., Taylor, C. J., Deng, W., Fivelman, Q. L., Cummings, R. M., Polley, S. D., Billker, O., and Baker, D. A. (2008) Gametogenesis in malaria parasites is mediated by the cGMP-dependent protein kinase. *PLoS Biol.* **6,** e139 CrossRef Medline
9. Govindasamy, K., Jebiwott, S., Jaijyan, D. K., Davidow, A., Ojo, K. K., Van Voorhis, W. C., Brochet, M., Billker, O., and Bhanot, P. (2016) Invasion of hepatocytes by *Plasmodium* sporozoites requires cGMP-dependent protein kinase and calcium dependent protein kinase 4. *Mol. Microbiol.* **102,** 349–363 CrossRef Medline
10. Miller, L. H., Ackerman, H. C., Su, X. Z., and Wellems, T. E. (2013) Malaria biology and disease pathogenesis: insights for new treatments. *Nat. Med.* **19,** 156–167 CrossRef Medline
11. Fairhurst, R. M. (2015) Understanding artemisinin-resistant malaria. *Curr. Opin. Infect. Dis.* **28,** 417–425 CrossRef Medline
12. Alam, M. M., Solyakov, L., Bottrill, A. R., Flueck, C., Siddiqui, F. A., Singh, S., Mistry, S., Viskaduraki, M., Lee, K., Hopp, C. S., Chitnis, C. E., Doerig, C., Moon, R. W., Green, J. L., Holder, A. A., *et al.* (2015) Phosphoproteomics reveals malaria parasite protein kinase G as a signalling hub regulating egress and invasion. *Nat. Commun.* **6,** 7285 CrossRef Medline
13. Diaz, C. A., Allocco, J., Powles, M. A., Yeung, L., Donald, R. G. K., Anderson, J. W., and Liberator, P. A. (2006) Characterization of *Plasmodium falciparum* cGMP-dependent protein kinase (PfPKG): antiparasitic activity of a PKG inhibitor. *Mol. Biochem. Parasitol.* **146,** 78–88 CrossRef Medline
14. Kim, J. J., Flueck, C., Franz, E., Sanabria-Figueroa, E., Thompson, E., Lorenz, R., Bertinetti, D., Baker, D. A., Herberg, F. W., and Kim, C. (2015) Crystal structures of the carboxyl cGMP binding domain of the *Plasmodium falciparum* cGMP-dependent protein kinase reveal a novel capping triad crucial for merozoite egress. *PLOS Pathog.* **11,** e1004639 CrossRef Medline
15. Collins, C. R., Hackett, F., Strath, M., Penzo, M., Withers-Martinez, C., Baker, D. A., and Blackman, M. J. (2013) Malaria parasite cGMP-dependent protein kinase regulates blood stage merozoite secretory organelle discharge and egress. *PLoS Pathog.* **9,** e1003344 CrossRef Medline
16. Cohen, P. (2002) Protein kinases—the major drug targets of the twenty-first century? *Nat. Rev. Drug Discov.* **1,** 309–315 CrossRef Medline
17. Baker, D. A., and Deng, W. (2005) Cyclic GMP-dependent protein kinases in protozoa. *Front. Biosci.* **10,** 1229–1238 CrossRef Medline
18. Kim, J. J., Lorenz, R., Arold, S. T., Reger, A. S., Sankaran, B., Casteel, D. E., Herberg, F. W., and Kim, C. (2016) Crystal structure of PKG I:cGMP complex reveals a cGMP-mediated dimeric interface that facilitates cGMP-induced activation. *Structure* **24,** 710–720 CrossRef Medline
19. Moon, T. M., Sheehe, J. L., Nukareddy, P., Nausch, L. W., Wohlfahrt, J., Matthews, D. E., Blumenthal, D. K., and Dostmann, W. R. (2018) An N-terminally truncated form of cyclic GMP–dependent protein kinase Iα (PKG Iα) is monomeric and autoinhibited and provides a model for activation. *J. Biol. Chem.* **293,** 7916–7929 CrossRef Medline
20. Deng, W., Parbhu-Patel, A., Meyer, D. J., and Baker, D. A. (2003) The role of two novel regulatory sites in the activation of the cGMP-dependent protein kinase from *Plasmodium falciparum. Biochem. J.* **374,** 559–565 CrossRef Medline
21. Franz, E., Knape, M. J., and Herberg, F. W. (2018) cGMP binding domain D mediates a unique activation mechanism in *Plasmodium falciparum* PKG. *ACS Infect. Dis.* **4,** 415–423 CrossRef Medline

ASBMB

22. Berman, H. M., Ten Eyck, L. F., Goodsell, D. S., Haste, N. M., Kornev, A., and Taylor, S. S. (2005) The cAMP binding domain: an ancient signaling module. *Proc. Natl. Acad. Sci. U.S.A.* **102,** 45–50 CrossRef Medline

23. Huang, G. Y., Kim, J. J., Reger, A. S., Lorenz, R., Moon, E. W., Zhao, C., Casteel, D. E., Bertinetti, D., Vanschouwen, B., Selvaratnam, R., Pflugrath, J. W., Sankaran, B., Melacini, G., Herberg, F. W., and Kim, C. (2014) Structural basis for cyclic-nucleotide selectivity and cGMP-selective activation of PKGi. *Structure* **22,** 116–124 CrossRef Medline

24. El Bakkouri, M., Kouidmi, I., Wernimont, A. K., Amani, M., Hutchinson, A., Loppnau, P., Kim, J. J., Flueck, C., Walker, J. R., Seitova, A., Senisterra, G., Kakihara, Y., Kim, C., Blackman, M. J., Calmettes, C., *et al.* (2019) Structures of the cGMP-dependent protein kinase in malaria parasites reveal a unique structural relay mechanism for activation. *Proc. Natl. Acad. Sci. U.S.A.* **116,** 14164–14173 CrossRef Medline

25. Monod, J., Wyman, J., and Changeux, J.-P. (1965) On the nature of allosteric transitions: a plausible model. *J. Mol. Biol.* **12,** 88–118 CrossRef Medline

26. Akimoto, M., Moleschi, K., Boulton, S., VanSchouwen, B., Selvaratnam, R., Taylor, S. S., and Melacini, G. (2014) Allosteric linkers in cAMP signalling. *Biochem. Soc. Trans.* **42,** 139–144 CrossRef Medline

27. Akimoto, M., Selvaratnam, R., McNicholl, E. T., Verma, G., Taylor, S. S., and Melacini, G. (2013) Signaling through dynamic linkers as revealed by PKA. *Proc. Natl. Acad. Sci. U.S.A.* **110,** 14231–14236 CrossRef Medline

28. VanSchouwen, B., Selvaratnam, R., Giri, R., Lorenz, R., Herberg, F. W., Kim, C., and Melacini, G. (2015) Mechanism of cAMP partial agonism in protein kinase G (PKG). *J. Biol. Chem.* **290,** 28631–28641 CrossRef Medline

29. Selvaratnam, R., VanSchouwen, B., Fogolari, F., Mazhab-Jafari, M. T., Das, R., and Melacini, G. (2012) The projection analysis of NMR chemical shifts reveals extended EPAC autoinhibition determinants. *Biophys. J.* **102,** 630–639 CrossRef Medline

30. Selvaratnam, R., Chowdhury, S., VanSchouwen, B., and Melacini, G. (2011) Mapping allostery through the covariance analysis of NMR chemical shifts. *Proc. Natl. Acad. Sci. U.S.A.* **108,** 6133–6138 CrossRef Medline

31. Akimoto, M., McNicholl, E. T., Ramkissoon, A., Moleschi, K., Taylor, S. S., and Melacini, G. (2015) Mapping the free energy landscape of PKA inhibition and activation: a double-conformational selection model for the tandem cAMP-binding domains of PKA RIα. *PLoS Biol.* **13,** e1002305 CrossRef Medline

32. Boulton, S., Akimoto, M., Akbarizadeh, S., and Melacini, G. (2017) Free energy landscape remodeling of the cardiac pacemaker channel explains the molecular basis of familial sinus bradycardia. *J. Biol. Chem.* **292,** 6414–6428 CrossRef Medline

33. Boulton, S., Selvaratnam, R., Blondeau, J.-P., Lezoualc'h, F., and Melacini, G. (2018) Mechanism of selective enzyme inhibition through uncompetitive regulation of an allosteric agonist. *J. Am. Chem. Soc.* **140,** 9624–9637 CrossRef Medline

34. Das, R., Chowdhury, S., Mazhab-Jafari, M. T., Sildas, S., Selvaratnam, R., and Melacini, G. (2009) Dynamically driven ligand selectivity in cyclic nucleotide binding domains. *J. Biol. Chem.* **284,** 23682–23696 CrossRef Medline

35. Rehmann, H., Arias-Palomo, E., Hadders, M. A., Schwede, F., Llorca, O., and Bos, J. L. (2008) Structure of Epac2 in complex with a cyclic AMP analogue and RAP1B. *Nature* **455,** 124–127 CrossRef Medline

36. Zagotta, W. N., Olivier, N. B., Black, K. D., Young, E. C., Olson, R., and Gouaux, E. (2003) Structural basis for modulation and agonist specificity of HCN pacemaker channels. *Nature* **425,** 200–205 CrossRef Medline

37. Su, Y., Dostmann, W. R., Herberg, F. W., Durick, K., Xuong, N. H., Ten Eyck, L., Taylor, S. S., and Varughese, K. I. (1995) Regulatory subunit of protein kinase A: structure of deletion mutant with cAMP binding domains. *Science* **269,** 807–813 CrossRef Medline

38. Clayton, G. M., Silverman, W. R., Heginbotham, L., and Morais-Cabral, J. H. (2004) Structural basis of ligand activation in a cyclic nucleotide regulated potassium channel. *Cell* **119,** 615–627 CrossRef Medline

39. Dolgova, N. V., Yu, C., Cvitkovic, J. P., Hodak, M., Nienaber, K. H., Summers, K. L., Cotelesage, J. J. H., Bernholc, J., Kaminski, G. A., Pickering, I. J., George, G. N., and Dmitriev, O. Y. (2017) Binding of copper and cisplatin to Atox1 is mediated by glutathione through the formation of metal–sulfur clusters. *Biochemistry* **56,** 3129–3141 CrossRef Medline

40. McNicholl, E. T., Das, R., SilDas, S., Taylor, S. S., and Melacini, G. (2010) Communication between tandem cAMP binding domains in the regulatory subunit of protein kinase A-Iα as revealed by domain-silencing mutations. *J. Biol. Chem.* **285,** 15523–15537 CrossRef Medline

41. Fayos, R., Melacini, G., Newlon, M. G., Burns, L., Scott, J. D., and Jennings, P. A. (2003) Induction of flexibility through protein-protein interactions. *J. Biol. Chem.* **278,** 18581–18587 CrossRef Medline

42. Delaglio, F., Grzesiek, S., Vuister, G. W., Zhu, G., Pfeifer, J., and Bax, A. (1995) NMRPipe: a multidimensional spectral processing system based on UNIX pipes. *J. Biomol. NMR* **6,** 277–293 CrossRef Medline

43. Goddard, T. D., and Kneller, D. G. (2006) *SPARKY, NMR Assignment and Integration Software*, version 3, University of California, San Francisco

44. Boulton, S., Akimoto, M., Selvaratnam, R., Bashiri, A., and Melacini, G. (2014) A tool set to map allosteric networks through the NMR chemical shift covariance analysis. *Sci. Rep.* **4,** 7306 CrossRef Medline

45. Selvaratnam, R., Mazhab-Jafari, M. T., Das, R., and Melacini, G. (2012) The auto-inhibitory role of the EPAC hinge helix as mapped by NMR. *PLoS One* **7,** e48707 CrossRef Medline

46. Cook, P. F., Neville, M. E., Jr., Vrana, K. E., Hartl, F. T., and Roskoski, R., Jr. (1982) Adenosine cyclic 3′,5′-monophosphate dependent protein kinase: kinetic mechanism for the bovine skeletal muscle catalytic subunit. *Biochemistry* **21,** 5794–5799 CrossRef Medline

47. Riniker, S., and Landrum, G. A. (2015) Better informed distance geometry: using what we know to improve conformation generation. *J. Chem. Inf. Model.* **55,** 2562–2574 CrossRef Medline

48. Morris, G. M., Huey, R., Lindstrom, W., Sanner, M. F., Belew, R. K., Goodsell, D. S., and Olson, A. J. (2009) AutoDock4 and AutoDockTools4: automated docking with selective receptor flexibility. *J. Comput. Chem.* **30,** 2785–2791 CrossRef Medline

49. Case, D. A., Betz, R. M., Cerutti, D. S., Cheatham, T. E., Darden, T., and Duke, R. E. (2016) *AMBER16*, University of California, San Francisco

50. Frisch, M. J., Trucks, G. W., Schlegel, H. B., Scuseria, G. E., Robb, M. A., Cheeseman, J. R., Scalmani, G., Barone, V., Mennucci, B., Petersson, G. A., Nakatsuji, H., Caricato, M., Li, X., Hratchian, H. P., Izmaylov, A. F., *et al.* (2016) *Gaussian 09*, revision E01, Gaussian, Inc., Wallingford, CT

51. Huang, J., Sun, B., Yao, Y., and Liu, J. (2017) Fast and reliable thermodynamic approach for determining the protonation state of the Asp dyad. *J. Chem. Inf. Model.* **57,** 2273–2280 CrossRef Medline

52. VanSchouwen, B., Selvaratnam, R., Fogolari, F., and Melacini, G. (2011) Role of dynamics in the autoinhibition and activation of the exchange protein directly activated by cyclic AMP (EPAC). *J. Biol. Chem.* **286,** 42655–42669 CrossRef Medline

53. Roe, D. R., and Cheatham, T. E., 3rd (2013) PTRAJ and CPPTRAJ: software for processing and analysis of molecular dynamics trajectory data. *J. Chem. Theory Comput.* **9,** 3084–3095 CrossRef Medline

54. Han, B., Liu, Y., Ginzinger, S. W., and Wishart, D. S. (2011) SHIFTX2: significantly improved protein chemical shift prediction. *J. Biomol. NMR* **50,** 43–57 CrossRef Medline